Classifying the hierarchy of nonlinear-Schrödinger-equation rogue-wave solutions

David J. Kedziora,* Adrian Ankiewicz, and Nail Akhmediev
Optical Sciences Group, Research School of Physics and Engineering, The Australian National University, Canberra ACT 0200, Australia
(Received 22 January 2013; revised manuscript received 28 March 2013; published 30 July 2013)

We present a systematic classification for higher-order rogue-wave solutions of the nonlinear Schrödinger equation, constructed as the nonlinear superposition of first-order breathers via the recursive Darboux transformation scheme. This hierarchy is subdivided into structures that exhibit varying degrees of radial symmetry, all arising from independent degrees of freedom associated with physical translations of component breathers. We reveal the general rules required to produce these fundamental patterns. Consequently, we are able to extrapolate the general shape for rogue-wave solutions beyond order 6, at which point accuracy limitations due to current standards of numerical generation become non-negligible. Furthermore, we indicate how a large set of irregular rogue-wave solutions can be produced by hybridizing these fundamental structures.

DOI: 10.1103/PhysRevE.88.013207 PACS number(s): 05.45.Yv, 47.20.Ky, 42.65.−k

I. INTRODUCTION

The nonlinear Schrödinger equation (NLSE) has become one of the most studied partial differential equations since its inception in the 1960s. A major part of this appeal stems from its wide variety of applications in various branches of physics. Indeed, the universality of this equation has resulted in many common phenomena being discovered in optics, oceanography, superfluids, and even atmospheric science. Of particular historical note, it was one of the first known integrable equations admitting the existence of solitons. Since then, their nonlinear superpositions with each other and with radiation have been intensively studied. More recently, significant attention has been directed to rogue-wave solutions. These are marked by brief "bursts" of large amplitude, localized in both space and time, on an otherwise quiescent background. This unique feature makes them effective prototypes for describing notorious rogue waves in the ocean [1,2]. Moreover, these solutions have found substantial utility in other fields of science where we find unexpected high-impact extreme events.

In addition to spatiotemporal localization, another main feature of this class of solutions is their hierarchical structure. The lowest-order solution is known as a Peregrine breather (or soliton) [3], which is described by a simple quasirational expression. The second-order solution was first introduced in 1985 [4] and has recently been presented again in the context of freak waves [5]. Further progress in revealing higher-order solutions has mostly revolved around the development of mathematical techniques that can ideally represent the whole set in explicit form. Certainly, the rational solutions require a special approach that differs from those used to obtain multisoliton solutions. Several methods have been considered in the quest for deriving the whole hierarchy [6–10], but there is no consensus to date that any one of them has an explicit advantage over the others. Moreover, despite much effort being placed into obtaining the hierarchy, we can conclude that there is currently no complete classification of higher-order rogue-wave solutions. Thus, continued investigation is required in order to better understand the rogue-wave phenomenon.

On the practical side, a series of recent experiments has shown that rogue waves can be produced in a water-based environment. The Peregrine breather, the second-order rogue wave, and solutions up to order 5 have been observed in experiments [11–13]. The Peregrine breather similarly has been generated in optics [14,15] and magnetoplasma [16,17]. Thus, the validity of the simplest rogue-wave solutions has been experimentally confirmed. This also means that the theoretical classification of the whole hierarchy of rogue waves is crucial for further developments in this area of research.

One significant discovery in this regard is that there are no higher-order solutions that are physically separable into 2,4,5,7,8,9, ... elementary Peregrine breathers. Their number is well defined [18,19] and given by the simple expression $n(n+1)/2$, where n is the order of the solution. Following this rule, we can have rogue-wave triplets, sextets, dectets, and so on [18–20], but composites of any other number are not allowed under the NLSE. Another important theoretical result is that these elementary parts of the higher-order rogue waves do not need to be localized at the same position but can be arrayed spatiotemporally in elegant geometries [9,10,19,20]. Nonetheless, despite the discovery of these interesting general facts, there is neither any systematic categorization of the NLSE rogue-wave hierarchy nor a description of how to routinely produce all geometric forms via any particular method. Search strategies may become particularly complicated when exact analytic solutions turn out to be too cumbersome to manipulate. In such a case, it naturally ensues that rogue-wave profiles must be investigated numerically.

This work is the continuation of our previous efforts in finding higher-order NLSE rogue-wave solutions [18–21]. It is based on the Darboux method [22], which remains an efficient technique despite the development of alternative methods. Most importantly, our present research is summative. It provides a classification that is a crucial step in predicting solutions from an infinite array of fundamental rogue-wave structures. The level of predictive power seen in our approach is a necessity in the present state of rogue-wave science, which faces a multiplicity of methods and a haphazard collection of particular solutions presented by various authors. Via the introduction of our scheme, we show that each solution is within easy numerical reach, while our classification is sufficient to indicate trends for higher-order solutions.

*Corresponding author: djk105@rsphysse.anu.edu.au

By nontrivially modifying parameters related to physical shifts in the scheme and relating them to frequency ratios of individual components, we have extended higher-order rogue-wave patterns beyond circular clusters [19] and triangular cascades [20]. Some of these new structures have been independently obtained via an alternative methodology [10]. Here we have modified the Darboux scheme used in our previous works. Namely, the technique is reconsidered using our new "polynomials of existence" concept. The reasoning behind this is twofold: it introduces what is arguably a complicated idea and also proves consistency with previous results. Section III of our present work shows that even "simple" rogue-wave structures comply with our newly found rule.

The rules governing these structures can be extrapolated far beyond the general solution of order 6, where numerical limitations start to be noticeable. Moreover, irregular rogue-wave solutions that also exist can now be interpreted as "hybridized" versions of the fundamental profiles obtained in the analysis. In this way, we, first, broaden and improve our current theoretical understanding of rogue waves and, second, set classification standards that may become useful in the analysis of rogue-wave hierarchies pertaining to related equations, such as the Hirota [23] or Sasa-Satsuma systems [24].

II. THEORY

We begin by expressing the dimensionless 1D NLSE as

$$i\frac{\partial\psi}{\partial x}+\frac{1}{2}\frac{\partial^2\psi}{\partial t^2}+|\psi|^2\psi=0, \tag{1}$$

with the wave envelope described by the complex function $\psi(x,t)$. The variables here are named in accordance with fiber optic convention [14,15], where x is the normalized distance along the fiber and t is the retarded time in the frame moving with the pulse group velocity. Alternatively, in water wave applications [11–13], x is interpreted as the normalized time while t is the distance in the frame moving with the group velocity. In either case, a simple linear transformation involving group velocity allows us to find the relation between both conventional forms and their variables. Perhaps a more important observation is the choice of particular coefficients in front of each term in Eq. (1), considering that this particular choice is responsible for the circular nature of emergent spatiotemporal patterns [19].

Clearly, the nonlinearity in the equation complicates routine analytic solving processes. Fortunately, to find involved solutions of Eq. (1), we can start with simple ones and build on them with the Darboux method. The technique is well described in the literature [22,25] and the specific formalism we use in this work has been expressly detailed previously [19,26]. It is also provided here in Appendix A. Conceptually, the procedure uses a seeding solution to the evolution equation, such as a plane wave ($\psi=e^{ix}$), and generates a first-order "building block." In this case, the fundamental component is a breather, from which all higher-order solutions can be constructed. For simplicity, we have fixed the amplitude of the seeding plane wave at 1 in this work, but it can always be made arbitrary after the final stage of construction via a scaling transformation [5].

It follows that a nonlinear superposition of order n requires n first-order components. Hence, we give the label j for each component, such that $1\leqslant j\leqslant n$. Each component can be translated by an amount x_j or t_j along the x or t axes, respectively. Most importantly, each first-order breather is governed by a complex eigenvalue l_j. The real part of this eigenvalue aligns the breather at a finite angle with the x and t axes while the imaginary part sets its amplitude. However, the modulation period for a NLSE breather depends on the ratio between breather and background amplitudes. Therefore, with the background plane wave restricted to amplitude 1, the imaginary part of the eigenvalue directly controls breather frequency. Additionally, we restrict ourselves to zero-angle alignment in this work, so we henceforth assume l_j is purely imaginary. Complex eigenvalues can still be easily deployed in the Darboux scheme [26], but this current restriction does allow the modulation frequency of a breather to be defined simply as $\kappa_j=2\sqrt{1+l_j^2}$.

When $0<\mathrm{Im}(l_j)<1$, the frequency κ_j is real. The resulting first-order solution, called an Akhmediev breather (AB), is localized in x and periodic in t. A nonlinear superposition of three such ABs parallel to each other is shown in Fig. 1(a). Alternatively, when $\mathrm{Im}(l_j)>1$ and the frequency κ_j is purely imaginary, the solution is called a Kuznetsov-Ma (KM) soliton. In contrast to the AB, it is localized in t but periodic in x. The KM soliton has been displayed individually in Fig. 1 of our previous work [19]. We mention again that, for the general case of complex l_j, the oscillating soliton is located at a finite angle to the x and t axes.

In each case, the modulation frequency can be controlled by the eigenvalue. The period of the AB solution increases when $\kappa_j\to 0$, as can be seen from the examples shown in Fig. 1. In the limit of $l_j\to i$ ($\kappa_j\to 0$), the period of both the ABs and KM solitons goes to infinity and, in the first-order scenario, only one isolated peak remains. Such a solution is known as a Peregrine soliton and is considered to be the prototype of a first-order rogue wave. In Fig. 1(c), which depicts a nonlinear superposition of three $\kappa_j\to 0$ ABs, six Peregrine solitons appear simultaneously.

For higher-order rogue-wave solutions, several facts have already been previously established:

(1) All nonlinear superpositions of ABs and KM solitons in the rogue-wave limit ($\kappa_j\to 0,\forall j$) are reduced to a pattern of peaks, with each appearing as a Peregrine soliton or some nonlinear combination thereof. Then, naturally, the first-order rogue wave can be effectively considered as a "quantum" of the whole structure [20].

(2) The number of such quanta in an order n solution is not n, as one would expect when applying ordinary knowledge of multisoliton theory. Contrary to these expectations, the number of such quanta is $n(n+1)/2$. Figure 1(c) is a direct confirmation of this simple rule, representing the case for $n=3$.

(3) In inverse scattering theory, no two components with unique j can coexist with equal eigenvalues l_j. When this happens, the solution is undefined. The case has to be considered as degenerate and a special technique has to be used to resolve the uncertainty [21]. One of the ways to deal with the common $\kappa_j\to 0$ limit in the multirogue-wave case is to assume that $\kappa_j=k_j\times\kappa$, with unique values of k_j for

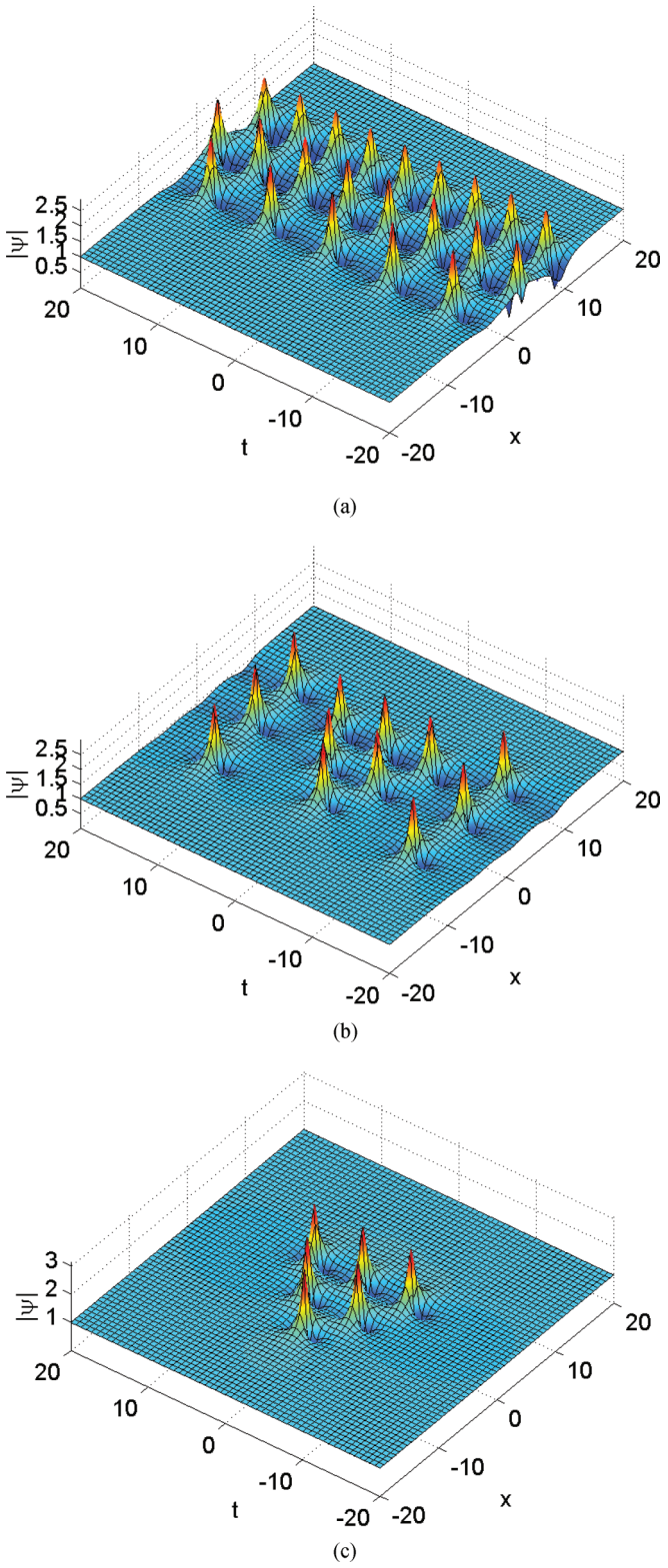

FIG. 1. (Color online) Step-by-step snapshots of the infinite-period limit applied to a triple AB superposition. Modulation frequencies are $\kappa_1 = \kappa$, $\kappa_2 = \sqrt{2}\kappa$, and $\kappa_3 = \sqrt{3}\kappa$. The shifts are $x_1 = 0, x_2 = 5\kappa^2$, and $x_3 = 10\kappa^2$. (a) $\kappa = 0.8$; (b) $\kappa = 0.5$; (c) $\kappa \approx 0$.

each j and with the ordering $k_1 < k_2 < \cdots < k_n$. As the common factor κ goes to zero, in the limit, all κ_j will be within the modulation instability band [26] no matter how many components are involved. From the successive changes leading to Fig. 1(c), we can conjecture that each component j contributes j rogue-wave quanta to the higher-order solution. This conjecture would justify the observed number of quanta, $n(n+1)/2$, in the whole superposition.

(4) Higher-order rogue-wave patterns are precariously dependent on the component shifts. An example is the third-order "triangular cascade" [20] shown in Fig. 1(c). Obtained from three ABs in the rogue-wave limit, this particular solution appears only when the shifts are scaled according to $x_j \propto \kappa^2$. If the shifts are proportional to other orders of frequency, the pattern changes. One such possibility (for $x_j \propto \kappa^4$) leads to a circular cluster [19]. More generally (e.g., for $x_j \propto \kappa^0$), the pattern may expand to the infinity horizon of the x and t plane when $\kappa \to 0$. A reduced number of peaks then will remain visible from the whole set. However, the remaining number of quanta should still be $i(i+1)/2$, where $i \leqslant n-2$ for an order n solution.

This fourth concept is highly unintuitive due to the intricacies of the rogue-wave limit. It motivates the unique redefinition of shifts as even-order expansions in the κ variable,

$$\begin{aligned} x_j &= \sum_{m=1}^{\infty} \kappa^{2(m-1)} X_{jm} \\ &= X_{j1} + X_{j2}\kappa^2 + X_{j3}\kappa^4 + \cdots, \\ t_j &= \sum_{m=1}^{\infty} \kappa^{2(m-1)} T_{jm} \\ &= T_{j1} + T_{j2}\kappa^2 + T_{j3}\kappa^4 + \cdots, \end{aligned} \tag{2}$$

where the coefficients X_{jm} and T_{jm} are constants. When $\kappa \to 0$, it follows that $x_j \to X_{j1}$ and $t_j \to T_{j1}$, i.e., all higher-order terms contribute negligibly to a physical component shift. Thus, one can mistakenly conclude that the extra shift coefficients have no impact on the NLSE rogue waves. However, analytic application of the rogue-wave limit shows that the values of the expansion coefficients are actually allowed to enter the solution [21]. Consequently, the structure of the resulting pattern depends on them.

When either X_{jn} or T_{jn} is nonzero for a single component in an order n solution, a basic higher-order rogue wave expels a ring of Peregrine solitons from the central structure. The solution then becomes a circular cluster [19]. However, in general, all expansion coefficients in Eq. (2) with $1 \leqslant m \leqslant n$ are important in determining the structure of an order n rogue wave, provided that the prelimit component frequencies are all in appropriate ratio. The triangular cascade in Fig. 1(c) is a prime example. It is a third-order solution, but it requires a certain ratio of $k_1 : k_2 : k_3$ and depends on the $m = 2$ expansion coefficients [20].

Below, we refer to the expansion coefficients X_{jm} as shifts of order m. For simplicity, we will set all $T_{jm} = 0$ unless otherwise stated. This does not affect the generality of our results as all rogue-wave patterns can be rotated in the x and t plane [20]. For these cases, the expansion coefficients of same order for x and t must be functionally related. In this work, we present all possible fundamental NLSE rogue-wave structures up to order 6, providing the relations between shifts

and frequencies that ensure their existence. By induction, we extend these patterns beyond order 6.

III. THE POLYNOMIALS OF EXISTENCE

The basic set of rogue-wave structures up to order 6 is shown in Fig. 2. Each image is a top-view false-color contour plot of an order n rogue wave constructed using only order m shifts. The latter mathematical restriction defines the basic set solutions (BSS). Section V gives further appearance-based justification for this natural choice of the BSS. Here, we present numerical evidence for how the structures of each column exist only if, for column m, there is a polynomial relation of order $m-1$ between the order m component shift values (X_{jm}) and the squared ratio coefficients of the modulation frequencies (k_j^2).

The images in the first column of Fig. 2 depict translations of traditional "fused" rogue waves [27], with the largest possible amplitude for each order n at the center of each wave function. The existence condition for such structures is simple: All components must have the same constant (or zero) shift. Nonzero shifts will simply translate the total structure in space and time from the origin. Any difference in the component shift values causes the solution to disappear. Specifically, the substructures that form the rogue wave in the $\kappa_j \to 0$ limit cannot coexist and repel each other to infinity, thus effectively reducing the order of the remnant composite rogue wave [19]. Therefore, the lowest-order shifts X_{j1} and T_{j1} must be equal for all j.

Rogue waves of order 4 are shown in Fig. 3(b). Three separate solutions are presented on the same plot to save space. The corresponding shift and frequency parameters for each solution are illustrated in Fig. 3(a). As discussed, all four components for each rogue wave must have the same X_{j1} value. The components must also have different prelimit modulation frequencies [21]. For example, rogue wave II has four components with a frequency ratio of $\kappa_1 : \kappa_2 : \kappa_3 : \kappa_4 = 1 : \sqrt{2} : \sqrt{3} : \sqrt{4}$, all with $X_{j1} = -5$. As a result, rogue wave II is located at $(x,t) = (-5,0)$ in Fig. 3(b). Choosing four coordinates on a line with a certain X_{j1} places the total structure at $x = X_{j1}$. This remains true if a component has a negative k_j^2 value, as it simply means that the prelimit ($\kappa \neq 0$) component frequency κ_j is imaginary. This is equivalent to saying that component 3 of rogue wave III was a KM soliton rather than an AB before application of the $\kappa \to 0$ limit.

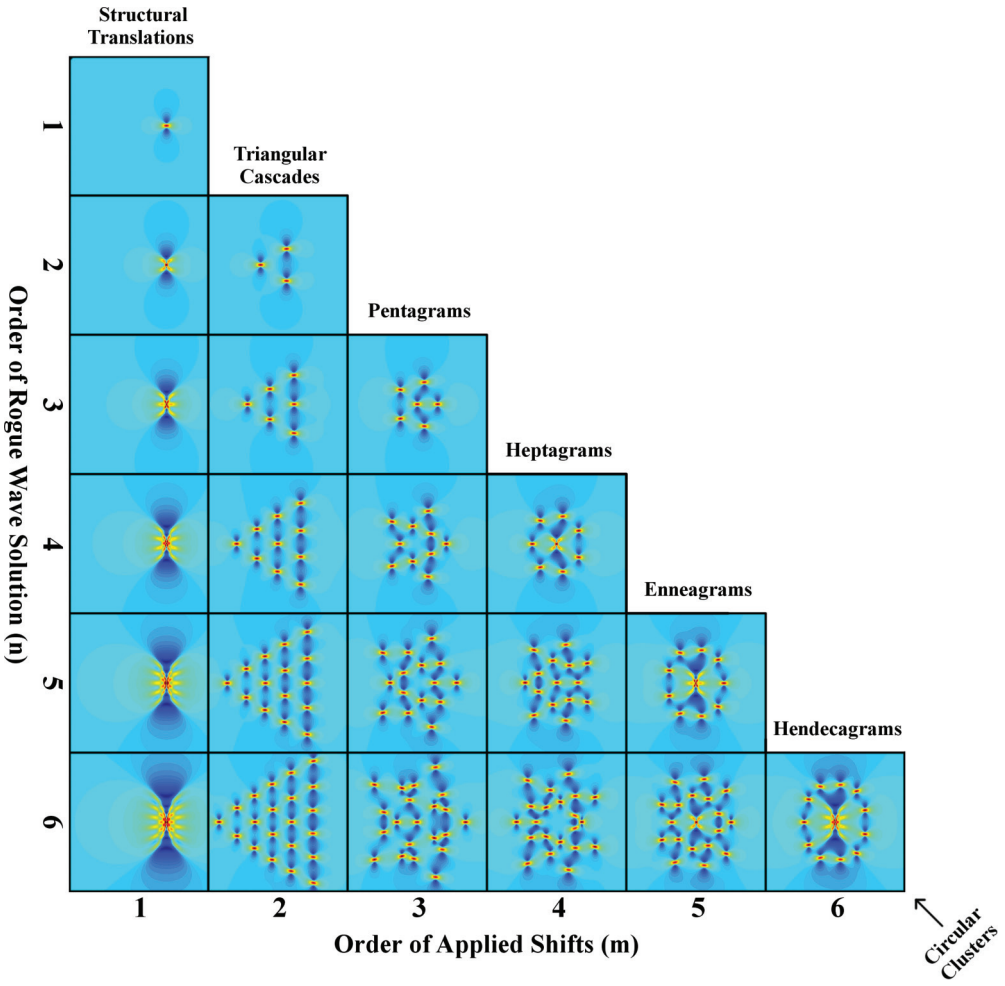

FIG. 2. (Color online) Overview of all fundamental rogue-wave solutions up to order 6. Structures in the first column appear off-center due to physical translations induced by first-order shifts. All other solutions are centered at the origin due to higher-order shifts being associated solely with fission effects. Structures belonging to column m (for $m > 1$) have effective radial symmetry of order $2m-1$. Each circular cluster along the diagonal ($n = m$) displays a ring of $2m-1$ Peregrine solitons around a central rogue wave of order $m-2$ (for $m > 2$).

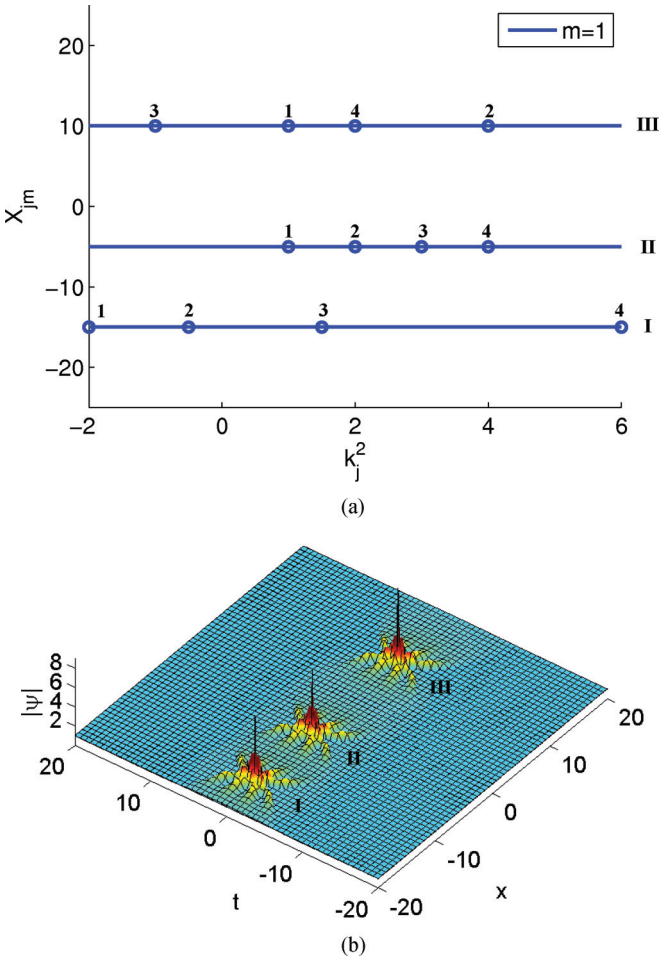

FIG. 3. (Color online) (a) Possible parameter choices for rogue waves of order 4 illustrated by circles. Vertical axis represents the first-order shift (X_{j1}) while the squared modulation frequency ratio coefficient (k_j^2) of each component is shown along the horizontal axis. The number above each circle is the component index (j). (b) A graphical superposition of the resulting rogue waves. Rogue waves I, II, and III are located at $x = X_{j1}$.

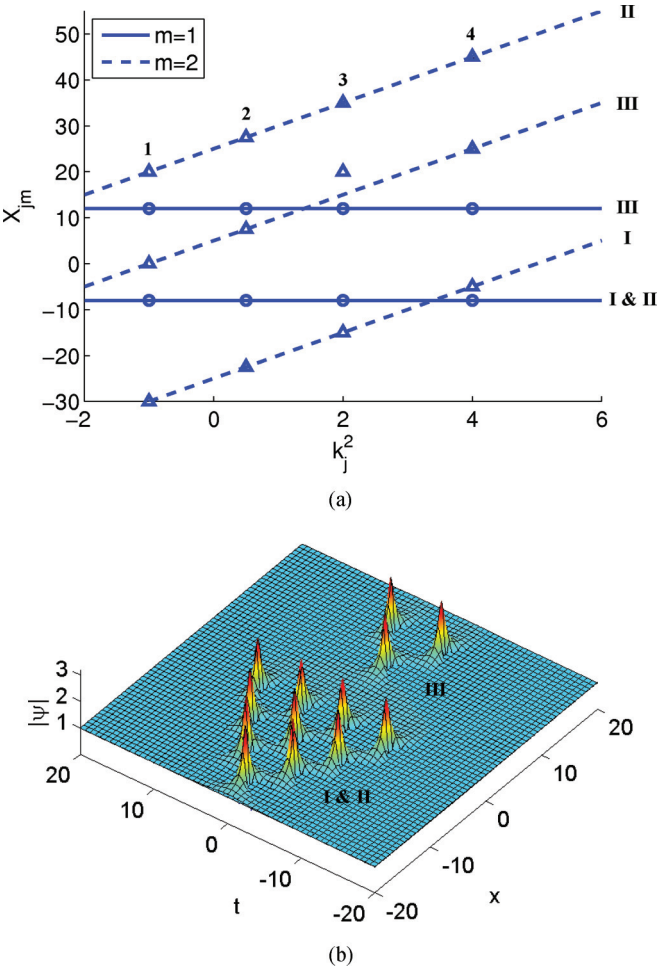

FIG. 4. (Color online) (a) Parameter choices for three instances of fourth-order rogue waves (I, II, and III). The components have the same squared modulation frequency ratio coefficients (k_j^2) for each of the three rogue waves. Thus, each column of coordinates is associated with a single component (denoted by index j). The ordinate of each circle and triangle is the first- and second-order shift (X_{j1} and X_{j2}), respectively, of each component. Lines represent the polynomial relations required for existence. (b) Overlay of resulting rogue waves I, II, and III. This is a graphical superposition of three different solutions, not a single solution. Two of them (I and II) are identical.

Similarly, rogue wave I forms in the intersection of two KM solitons and two ABs. Furthermore, the ordering of component frequencies is arbitrary. It does not have to be monotonic with respect to component index. Rogue wave III in Fig. 3 is an example of this.

The second column in Fig. 2 illustrates the simplest cases when higher-order shifts result in nontrivial structures. With various forerunners elsewhere [9,28], these triangular cascades were investigated in detail within our previous work [20]. It was found that these structures could be generated via the Darboux method with X_{j2} shifts alone. In particular, with the ordering $X_{12} < X_{22} < \cdots < X_{n2}$, and d_j denoting the second-order "differential shift" between the components j and $j+1$, a rogue-wave cascade is always produced in the $\kappa \to 0$ limit, provided that

$$\kappa_j : \kappa_{j+1} : \kappa_{j+2} = k_j : k_{j+1} : \sqrt{\frac{(d_j + d_{j+1})k_{j+1}^2 - d_{j+1}k_j^2}{d_j}}, \tag{3}$$

for all j ranging from 1 to $n-2$. It is evident that Eq. (3) is nothing but a linear relationship between the squared modulation frequency ratio coefficients (k_j^2) and second-order shifts. Indeed, Fig. 4 shows how triangular cascades can be constructed with adherence to this rule.

Standard fused rogue waves, such as those shown in Fig. 3(b), implicitly have X_{j2} set to zero for all j. This would be represented by a dashed $y = 0x + 0$ line in Fig. 3(a). If this line is modified in parameter space, as shown in Fig. 4(a), a higher-order rogue wave splits into a triangular array of Peregrine solitons. The y intercept of each line does nothing to affect the structure. Rogue waves I and II, translated to $x = -8$, have second-order shifts that lie on a $y = 5x - 25$ and $y = 5x + 25$ line, respectively. Yet the overlay in Fig. 4(b) shows that the two wave functions remain identical. On the

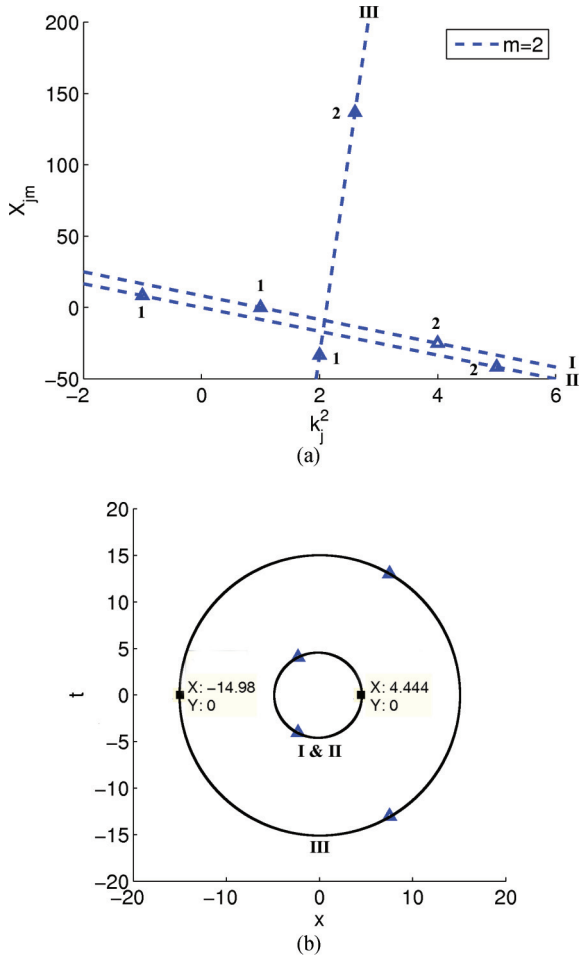

FIG. 5. (Color online) (a) Parameter choices for three rogue waves (I, II, and III) of order 2, shifted by X_{j2} alone. Coordinates of each triangle represent the second-order shift (X_{j2}) and the squared modulation frequency ratio coefficient (k_j^2) of each component, where the number near the triangle is the component index (j). Lines represent the polynomial relation required for existence. (b) The maxima of rogue waves I, II, and III in the x and t plane. Circumcircles are drawn for each triangular cascade.

other hand, it is crucial that all components have shifts that lie on the same polynomial of existence.

Rogue wave III is an example of where the rule is broken, with the value of X_{32} being five dimensionless units greater than what is required. This is represented in Fig. 4(a) by a triangular marker deviating from the dashed line denoted as III. As discussed with first-order shifts, the resulting structure is shown in Fig. 4(b) as a diminished rogue wave of second order. Moreover, this reduction in order is instantaneous in the $\kappa \to 0$ limit for any deviation. It appears necessary that any shifts belonging to a particular order must lie exactly on the relevant existence polynomial in parameter space.

Notably, the existence polynomial for second-order shifts has an extra degree of freedom relative to the one for first-order shifts, this being the slope of the line. In the case of Fig. 4(b), all three rogue waves are oriented in the same direction, due to the positive gradients of the $m = 2$ lines in Fig. 4(a). However, as the slope decreases to zero, the peaks merge together to form a fused rogue wave. If the gradient becomes negative, as with rogue waves I and II in Fig. 5(a), the solution again expands into a cascade but is now oriented in the opposite direction, as the three peaks in the center of Fig. 5(b) demonstrate.

To ensure consistency with previous work [18,19], we note that the circumradius of a second-order cascade (and cluster) was derived as

$$R \approx 2^{2/3}\left(x_d^2 + t_d^2\right)^{1/6}, \tag{4}$$

where $x_d = X_{12} - X_{22}$ and $t_d = T_{12} - T_{22}$. However, it was realized in later work that the scaling of shifts depends on the component frequencies established before the $\kappa \to 0$ limit [21]. This means that Eq. (4) is valid for a $\kappa_1 : \kappa_2 = 1{:}2$ ratio, used in the original analytic derivations, but must be recalculated for other prelimit ratios.

To demonstrate this, rogue wave I in Fig. 5(a) uses the original frequency ratio and has a value of 25 for x_d. The resulting circumradius, shown in Fig. 5(b), is $R \approx 4.444$, which is in reasonable agreement with the expected 4.6416 value. However, rogue wave II possesses a larger x_d value for a different prelimit frequency ratio and produces an identical wave function. In any case, the linear nature of the existence polynomial means that Eq. (4) can be used to engineer structures of any radius. Indeed, the second-order shifts of rogue wave III in Fig. 5(a) lie on the line $y = (850/3)x - 600$, which corresponds to $x_d = 850$ for the definitions used in Eq. (4). Accordingly, the circumradius of cascade III is approximately 15 in Fig. 5(b), as expected.

IV. PENTAGRAMS AND BEYOND

In the previous section, we established that an order $m - 1$ polynomial relationship between order m shifts and the squared ratio coefficients of component modulation frequencies results in both rogue-wave translations ($m = 1$) and cascades ($m = 2$). Deviations from these polynomials produce rogue waves of decreased order. However, both traditional fused structures [27] and cascades [9,20] are relatively well known at this stage. Fortunately, the aforementioned existence polynomials indicate a way to predictably generate more complicated structures that have only been glimpsed via other methods [10].

For example, forming a parabolic relationship between third-order shifts and k_j^2 is the natural next step, as shown in Fig. 6(a). Indeed, applying this polynomial restriction expands a standard fused rogue wave into a structure with effective pentaradial symmetry, shown for fourth order in Fig. 6(b), which we refer to as a rogue-wave pentagram. The top view of this wave function is the second image of the third column in Fig. 2.

As should be evident by this stage, it is only the order $m - 1$ derivative of the order $m - 1$ existence polynomial for X_{jm} that has any effect on the shape of the rogue wave. In the case of Fig. 6(a), all three parabolic curves have the same curvature for the same k_j^2 value, despite generally differing on slope and X_{jm} value. Consequently, the three rogue-wave pentagrams are identical in Fig. 6(b). However, as expected, the pentagram can be expanded in spatiotemporal size by choosing a parabola with increased curvature, and a vertically inverted

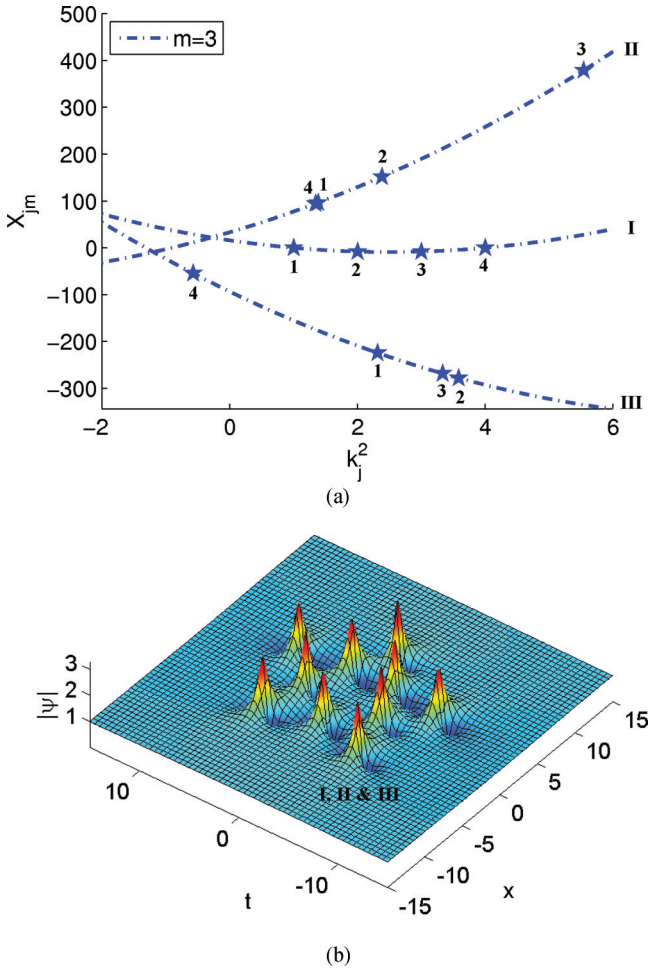

(a)

(b)

FIG. 6. (Color online) (a) Parameter choices for three rogue waves (I, II, and III) of order 4, shifted by X_{j3} alone. Coordinates of each star represent the third-order shift (X_{j3}) and the squared modulation frequency ratio coefficient (k_j^2) of each component, where the number near the star is the component index (j). Curves represent the polynomial relation required for existence. (b) Overlay of resulting rogue waves I, II, and III. This is a graphical superposition, but, as all three rogue waves are identical, this can also be considered a true solution.

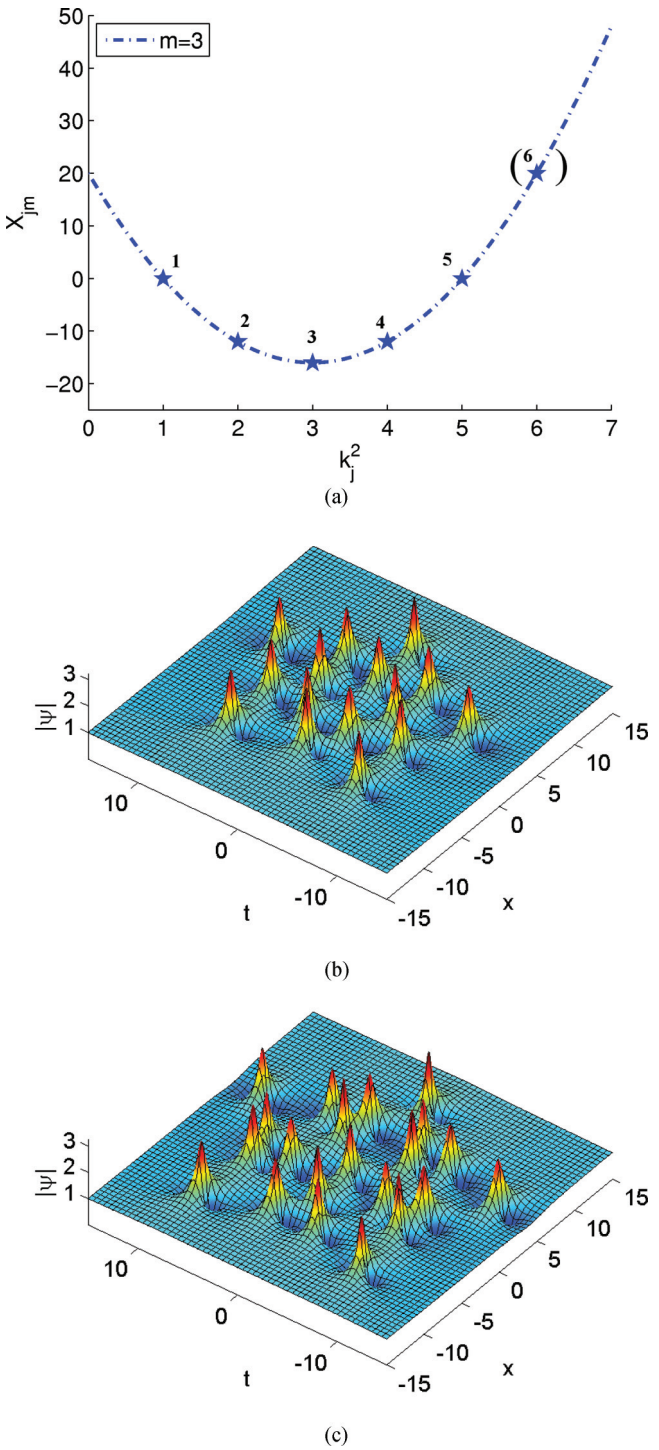

(a)

(b)

(c)

FIG. 7. (Color online) (a) Parameter choices for high-order rogue-wave pentagrams produced by X_{j3} shifts alone. Coordinates of each star represent the third-order shift (X_{j3}) and the squared modulation frequency ratio coefficient (k_j^2) of each component, where the number near the star is the component index (j). Curves represent the polynomial relation required for existence. (b) An order 5 pentagram generated with components 1 to 5. (c) An order 6 pentagram generated with components 1 to 6.

polynomial generates a pentagram that points in the opposite direction.

In general, the procedure for generating higher-order structures with pentaradial symmetry is to continue choosing extra components that adhere to the parabolic relation between third-order shifts and k_j^2. For example, Fig. 7(a) shows five components that obey the relation, thus producing the rogue-wave pentagram in Fig. 7(b), which is also displayed elsewhere [10]. However, Fig. 7(a) also shows a sixth component on the same existence polynomial, which contributes to the sixth-order pentagram in Fig. 7(c) being formed from six $\kappa \to 0$ ABs. Therefore, along with the similar extension of cascade forms [20], it is not hard to produce pentagram structures of any order.

The structures within each successive column of Fig. 2 follow the same trend. Second-order shifts are associated with triradial symmetry and triangular cascades, third-order shifts are associated with pentaradial symmetry and pentagrams, and, hence, order m shifts are associated with peak arrangements that are effectively identical following rotations of $2\pi/(2m-1)$. Rogue-wave heptagrams thus are generated

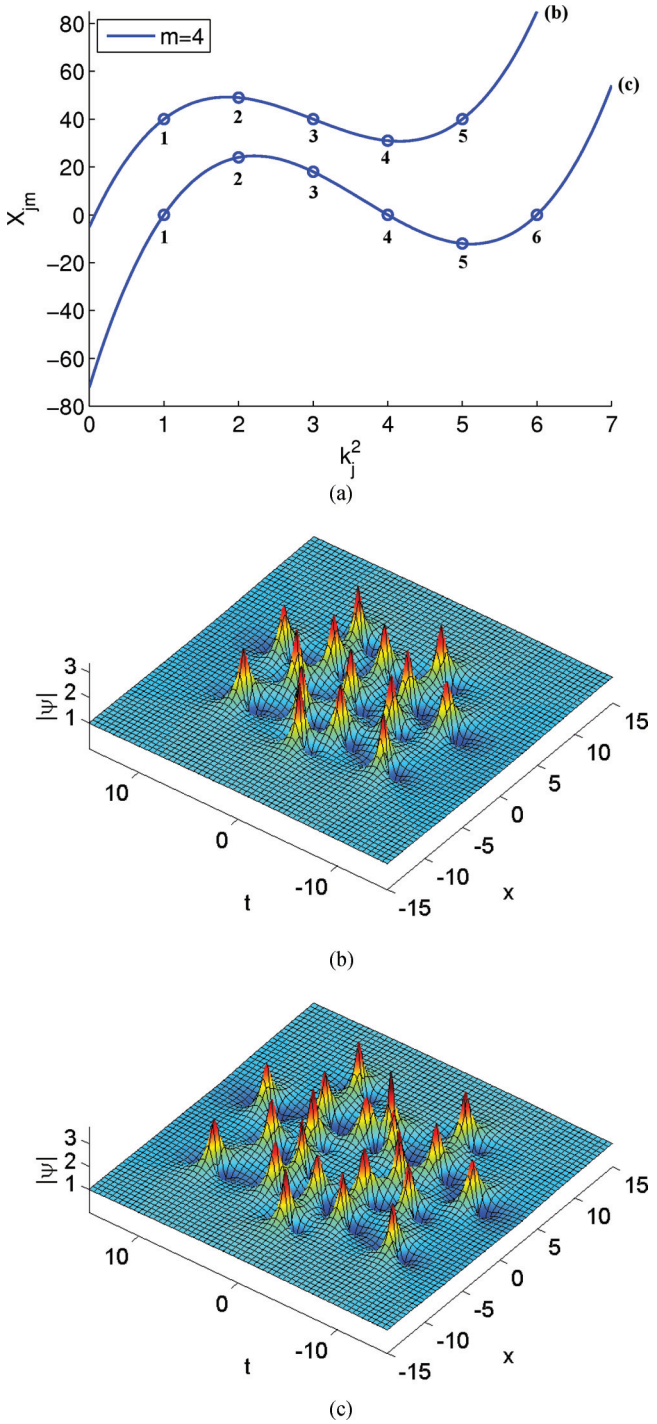

FIG. 8. (Color online) (a) Parameter choices for high-order rogue-wave heptagrams produced by X_{j4} shifts alone. Coordinates of each circle represent the fourth-order shift (X_{j4}) and the squared modulation frequency ratio coefficient (k_j^2) of each component, where the number near the circle is the component index (j). Curves represent the polynomial relation required for existence. (b) Rogue wave of order 5. (c) Rogue wave of order 6.

from cubic relations involving squared component frequencies and fourth-order shifts, as shown in Fig. 8(a). As usual, only the fourth-order derivative of the polynomial appears to have any effect on structural spacing. A rogue-wave heptagram recursively generated from five ABs is shown in Fig. 8(b), while a sixth-order heptagram is shown in Fig. 8(c). The limits of numerical accuracy lead to a minor distortion of shape in the latter case, but both wave functions still display concentric rings, each with seven rogue-wave quanta.

This existence polynomial technique can be extended indefinitely, with a quartic relationship between X_{j5} and k_j^2 in Fig. 9(a) leading to the generation of rogue-wave enneagram I in Fig. 9(b). In combination with previous circular cluster [19] and triangular cascade results [20], these new solutions cover all the fundamental structures up to order 6, as displayed in

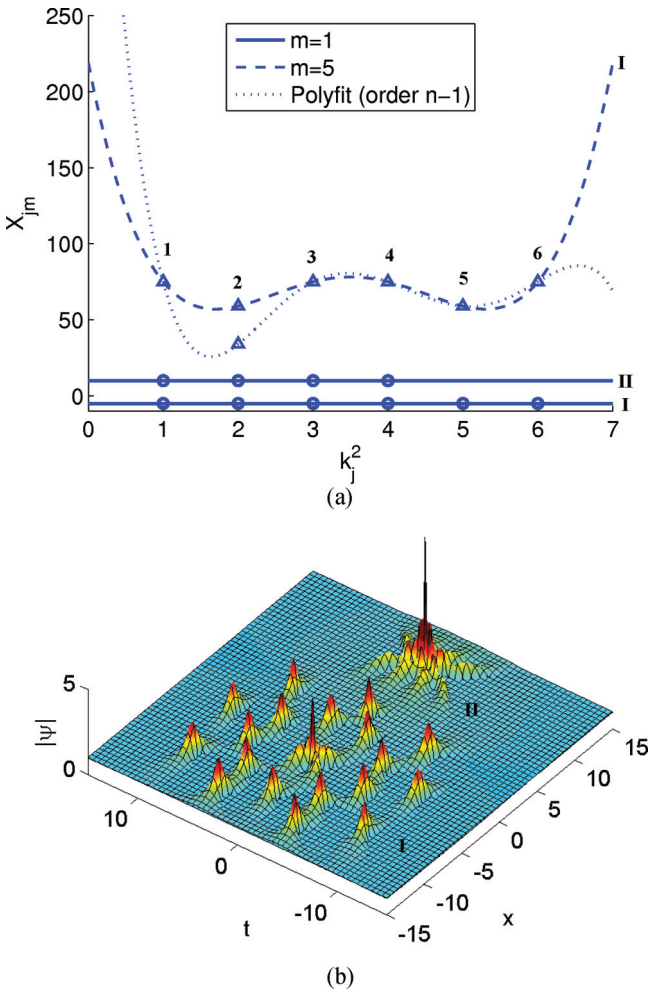

FIG. 9. (Color online) A rogue wave of order 6, shifted by X_{j1} and X_{j5} alone, and a rogue wave of order 4, shifted by X_{j1} alone. (a) Parameter choices for rogue waves I and II. The components (where they exist) have the same squared modulation frequency ratio coefficients (k_j^2) for each of the two rogue waves. Thus each column of coordinates is associated with a single component (denoted by index j). The ordinate of each circle and triangle is the first- and fifth-order shift (X_{j1} and X_{j5}) of each component, respectively. Continuous lines and dashed curves represent the polynomial relations required for existence. The dotted line represents an order 5 polynomial fit of the X_{j5} shifts for rogue wave I when component 2 is perturbed. (b) Overlay of resulting rogue waves I and II. This is a graphical superposition, not a true solution.

Fig. 2. However, this understanding can be extended even further for higher orders and "hybrids."

V. EXTRAPOLATION AND HYBRIDIZATION

By associating each fundamental type of rogue-wave solution with a unique well-defined parameter in the Darboux generation scheme, we can visualize the trends in Fig. 2 and extend the patterns beyond order 6. We already know from Sec. IV that an order m shift is associated with radial symmetry of degree $2m-1$, which allows for the natural subdivision of fundamental solutions based on appearance. Moreover, the simplest nontrivial structure of any shift order appears to be a circular cluster, which is consistent with the notion of having $2m-1$ rogue-wave quanta in a ring [19]. Hence, we know that an order n structure with order n shifts alone will display an order $n-2$ peak (with amplitude $2n-3$) surrounded by $2n-1$ Peregrine solitons.

Conveniently, the existence polynomial theory explains why rogue waves are susceptible to shedding a ring of rogue-wave quanta for poorly chosen shifts. If we only let one order of shift be nonzero for all components, thus writing $x_j = X_{jm}\kappa^{2(m-1)}$, then this can always be expressed in terms of order n shifts, specifically $x_j = X_{jm}\kappa^{2(m-n)}\kappa^{2(n-1)}$, which in turn implies $X_{jn} = X_{jm}\kappa^{-2(n-m)}$. If X_{jm} is well chosen so as to adhere to the relevant existence polynomial, then we can consider it a finite contribution to a noncluster fundamental shape, such as in the case of fifth-order shifts in Fig. 9(a) producing the enneagram in Fig. 9(b). However, if X_{jm} fails to contribute in this way, such as by one component being perturbed from the existence polynomial, then the shifts must still have an effect of some sort. Indeed, there will always be an order $n-1$ polynomial that is capable of fitting n coordinates in parameter space, as shown in Fig. 9(a), which means that any "badly" generated structure will always default to circular cluster form. But as X_{jm} is nonzero and $n > m$, $\kappa \to 0$ will take all X_{jn} to infinity via the aforementioned relation. This effectively becomes an infinite contribution to a circular cluster shape, which manifests as a structure with infinite radius for its outer ring [19]. Thus, in such a case, an order $n-2$ structure is always left behind in the rogue-wave limit. For example, a perturbation of frequency or shift for enneagram I in Fig. 9(b) results in a fourth-order rogue wave similar to II.

Acknowledging this issue, we henceforth assume that shift orders adhere strictly to existence polynomials, resulting in finite contributions to relevant structures. The $n(n+1)/2$ rogue-wave quanta that constitute the structures of order n in Fig. 2 can then be subdivided into rings of $2m-1$ quanta, for sufficiently large shifts of order m, and a remnant that appears as a fused central peak. It is soon evident from Table I that certain patterns arise for increasing solution orders. For instance, the number of rogue-wave quanta in the center of a triangular cascade cycles through (0,1,0) for each successive triplet of solution order, starting with 0, 1, and 2. It follows that the center of a pentagram cycles through (0,1,3,1,0) merged rogue-wave quanta, and a heptagram center similarly cycles forwards and backwards between a zero- and third-order rogue wave. For this same reason, the enneagram in Fig. 9(b) is not solely composed of first-order Peregrine solitons. We thus can extrapolate that structures related to an order m shift iterate through cycles of length $2m-1$, where the central peak oscillates between a rogue wave of order 0 and $m-1$.

TABLE I. The structure of rogue wave arrays for various orders and shifts. The first column denoted as S.O. is the solution order. The second column (Qu.) denotes the number of rogue-wave quanta in the solution. The rest of the columns on the right, marked as SAm, show how the structure is arrayed when the order m shifts are sufficiently large. The elements of these columns are presented in the format $q_r \times r + q_c$, where q_r is the number of quanta per "ring," r is the number of rings, and q_c is the number of quanta fused into a central peak. Data beyond the solution of order 6 have been extrapolated.

S.O.	Qu.	SA1	SA2	SA3	SA4	SA5
0	0	**0**	$3\times0+$**0**	$5\times0+$**0**	$7\times0+$**0**	$9\times0+$**0**
1	1	**1**	$3\times0+$**1**	$5\times0+$**1**	$7\times0+$**1**	$9\times0+$**1**
2	3	**3**	$3\times1+$**0**	$5\times0+$**3**	$7\times0+$**3**	$9\times0+$**3**
3	6	**6**	$3\times2+$**0**	$5\times1+$**1**	$7\times0+$**6**	$9\times0+$**6**
4	10	**10**	$3\times3+$**1**	$5\times2+$**0**	$7\times1+$**3**	$9\times0+$**10**
5	15	**15**	$3\times5+$**0**	$5\times3+$**0**	$7\times2+$**1**	$9\times1+$**6**
6	21	**21**	$3\times7+$**0**	$5\times4+$**1**	$7\times3+$**0**	$9\times2+$**3**
7	28	**28**	$3\times9+$**1**	$5\times5+$**3**	$7\times4+$**0**	$9\times3+$**1**
8	36	**36**	$3\times12+$**0**	$5\times7+$**1**	$7\times5+$**1**	$9\times4+$**0**
9	45	**45**	$3\times15+$**0**	$5\times9+$**0**	$7\times6+$**3**	$9\times5+$**0**
10	55	**55**	$3\times18+$**1**	$5\times11+$**0**	$7\times7+$**6**	$9\times6+$**1**
. . .	. . .	. . .	. . .	. . .	. . .	. . .

It is also clear from Table I that the number of rings added per solution order increases by one after the point in every cycle where the center reaches maximum order. For instance, cascades begin adding individual triplets at order 2 and pairs of triplets at order 5. Consistent with this, the single-ring circular cluster happens to occur immediately following the maximum of the very first cycle, thus also explaining its order $m-2$ central peak. By combining all these trends, we can predict the layout of any fundamental rogue-wave solution affected by shifts. For example, an order 18 hendecagram, generated by order 6 shifts, should have a central third-order rogue-wave peak surrounded by 15 rings of 11 quanta each.

All this discussion of shape is fundamental to understanding the physics of rogue-wave NLSE structures. For one thing, maximum amplitudes of each solution and shift order are already implicitly encoded in Table I. For example, an order 7 pentagram (SA3 column) has a central peak of three fused quanta, which can be correlated with a second-order rogue wave via the SA1 column. Knowing that an order n fused rogue wave has an amplitude of $2n+1$, this means that the structure possesses a sharp spike of amplitude 5. Furthermore, with the information presented in this work, it is also possible to extrapolate backwards from shape so as to determine how many breathers are interacting to form a rogue wave and how they are spatiotemporally located with respect to each other.

This backward extrapolation becomes particularly relevant with the realization that experimentally produced NLSE rogue-wave structures are unlikely to ever truly be ideal. This means that κ in Eq. (2) is small but not zero, and both modulation frequencies and the different orders of shift manifest as actual physical observables pertaining to component breathers rather than mere theoretical abstractions. Moreover, as demonstrated

in the simplest case within Sec. III, the circumradius of a rogue wave "ring" is dependent on the highest-order coefficient of an existence polynomial. With the appropriate constant of proportionality determined, these results enable an effective bijection between simple breather arrangements and complex rogue waves of any spatiotemporal size.

In any case, we have thus far only discussed rogue waves associated with unique orders of shift in Eq. (2), having referred to them as "fundamental" structures (BSS) that obey the NLSE. However, the effects of different shift orders are independent, associating the set of X_{jm} and T_{jm}, for all j and for each $m \leqslant n$, with a degree of freedom in the determination of rogue-wave shape. This has been implied to some extent by Figs. 4 and 9, where X_{j1} has shifted entire wave functions without destabilizing the arrangements generated by other orders of shift. However, previous work with "claw structures" [20] has shown that this is not exclusive to first order, and any combination of fundamental wave functions can be mixed to generate a nontrivial hybrid rogue wave with shared features.

We originally postulated that single-ring clusters could be further split into multiple rings, with consecutive concentric shells differing by four Peregrine solitons [19]. Such an arrangement is nothing more than circular clusters within circular clusters, and this is achieved by making X_{jm} adhere to a nonzero order $m-1$ polynomial for $m = n, n-2$, $n-4, \ldots$, all the way down to second or third order. The only technicality is that each higher-order shift must be sufficiently large to pull out a ring of quanta. Due to the relative parametric ease by which circular clusters are generated, examples of the resulting multiring structures can be seen elsewhere [10]. Moreover, circular clusters are simple to hybridize in general. With sufficiently large X_{jn} and T_{jn} for an order n rogue wave, the central peak can be modified independently of the ring by any order of shift from 2 to $n-2$. For example, a sixth-order circular cluster, generated with nonzero T_{j6}, has its central peak arrayed into a fourth-order cascade via nonzero T_{j2}. This is shown in Fig. 10(a). Alternatively, the center can instead become a fourth-order pentagram via nonzero T_{j3}, as shown in Fig. 10(b).

This concept of decomposition has been independently verified elsewhere [10], but, because of the existence polynomial and hybridization theory outlined here, we can systematically extend this to construct many more unexpected NLSE rogue-wave solutions. It is clear that circular cluster hybrids are relatively simple to understand and extrapolate. The outermost ring draws out $2n-1$ rogue-wave quanta from $n(n+1)/2$, and leaves behind $(n-2)(n-1)/2$ quanta that can be rearranged into any order $n-2$ structure. However, if the highest order of nonzero shift is below n, then there is an attempt to exclude less than $2n-1$ quanta in a circular ring, which leaves behind an irregular number of quanta in the center. If left as a fundamental structure, the resulting rogue-wave arrangement is still regular and circular, as shown in Fig. 2. But hybridizing structures in general will result in a competition between features, only won decisively if one order of shift dominates the other. The higher degrees of symmetry will often break, resulting in bilateral rogue-wave arrangements [20]. Despite this, there are many hybrid structures that display elegant geometries. For example, a T_{j2} triangular cascade and a T_{j5} enneagram both

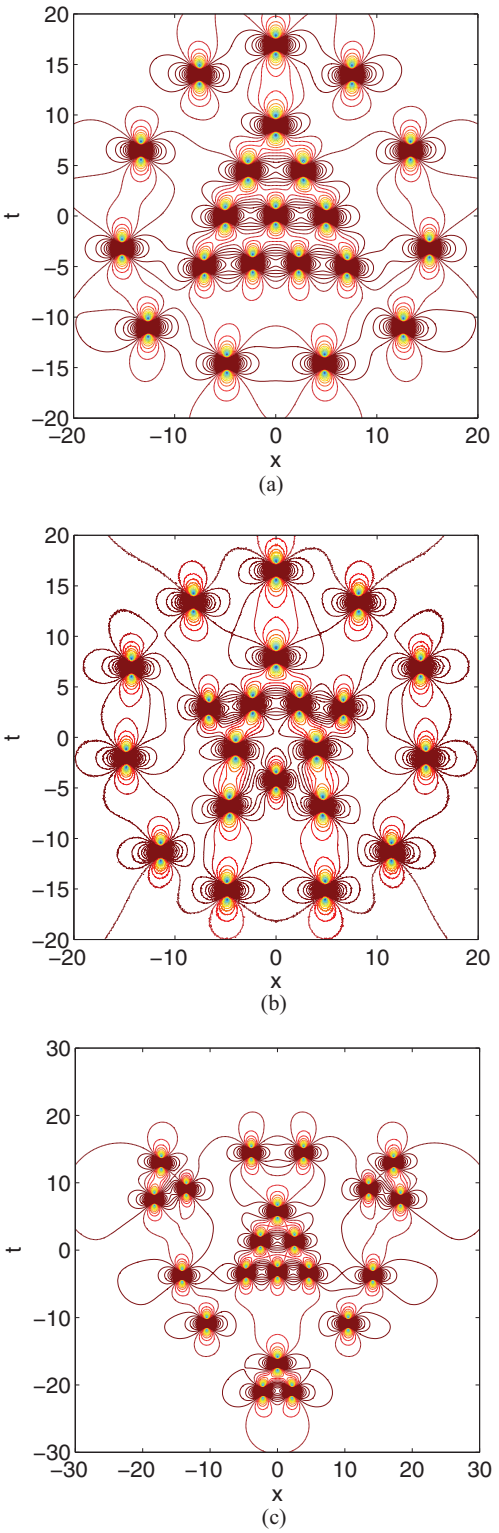

FIG. 10. (Color online) Contour plots of sixth-order hybrid rogue waves, shifted in the t axis, with $k_j = \sqrt{j}$. (a) Ringed cascade. T_{j2} and T_{j6} adhere to $y = 3.75(x-1)$ and $y = 1750(x^5 - 20x^4 + 155x^3 - 580x^2 + 1044x - 720)$, respectively, with respect to squared modulation frequency ratio coefficients (k_j^2). (b) Ringed pentagram. T_{j3} adheres to $y = 1.5(4x^2 - 28x + 24)$ with respect to k_j^2. T_{j6} is the same as for the ringed cascade. (c) Cascade-enneagram hybrid. T_{j2} and T_{j5} adhere to $y = -20(x-1)$ and $y = 500(2x^4 - 28x^3 + 134x^2 - 252x + 144)$, respectively, with respect to k_j^2.

share triradial symmetry. Thus, as Fig. 10(c) shows, mixing the structures retains that symmetry.

VI. CONCLUSION

In summary, our main results are as follows:

(1) Within the context of the Darboux scheme, we have shown that spatial and temporal axis shifts of breather components can be written as expansions involving frequency, and each coefficient within the expansion is responsible for a unique form of fundamental rogue-wave solution to the NLSE. We have named these coefficients "shifts of order m," whereby $m = 1$ is responsible for global structure translations, $m = 2$ is responsible for triangular cascades [20], $m = 3$ is responsible for pentagrams, and so on, as detailed in Fig. 2. For a rogue wave composed of n breathers, the $m = n$ shift is associated with a circular cluster [21]. Higher-order shifts beyond this do not appear to affect the structure of a rogue wave.

(2) We have shown numerically that, for rogue-wave structures of shift order $m < n$ to exist without defaulting to a circular cluster with infinite circumradius, the shifts of order m must fit a polynomial of order $m - 1$ with respect to the squared coefficients of the ratio between prelimit component frequencies. The spatiotemporal size of the resulting rogue-wave arrangement is determined by the order $m - 1$ derivative of the polynomial, but no other derivative appears to have any effect. The sign and ordering of ratio coefficients similarly do not affect the shape of the rogue wave.

(3) We have found that the arrangements of fundamental rogue-wave solutions have a radial symmetry of degree $2m - 1$ for shift orders $m > 1$. The wave functions form spatiotemporal concentric rings, each made from a multiple of $2m - 1$ Peregrine solitons, and any remaining quanta fuse in the center to appear as a rogue wave of up to order $m - 1$. Using the trends shown in Table I, we are, hence, able to extrapolate and predict the large-scale structure of extreme high-order rogue waves.

(4) By realizing that each coefficient of the shift expansion is an independent degree of freedom in determining rogue-wave arrangement, we are able to continue generating valid NLSE solutions by "hybridizing" fundamental structures associated with different orders of shift. Indeed, provided that one order of shift does not dominate another, the resulting wave function expresses features from all fundamental constituents. Circular clusters are particularly amenable to hybridization, with additional lower-order shifts modifying the central peak in regular fashion. However, other elegant geometries are also possible when radial symmetries share a common factor in degree beyond bilateral symmetry.

Our study shows that the world of rogue waves is significantly more complicated than the world of solitons. Their growth-decay cycle in both space and time makes them unique formations in physics, with a range of applicability that still waits to be discovered. At the very least, their intricate spatiotemporal structure makes them attractive objects of study from an aesthetic point of view. As of such, the world of rogue waves can be considered a fusion of art and science.

ACKNOWLEDGMENTS

The authors acknowledge the support of the Australian Research Council (Discovery Project number DP110102068). N.A. and A.A. acknowledge support from the Volkswagen Stiftung.

APPENDIX: THE DARBOUX METHOD

The NLSE in Eq. (1) can be written in Lax pair form (e.g., see Chap. 2 of Ref. [29]):

$$\frac{\partial R}{\partial t} = UR, \quad \frac{\partial R}{\partial x} = VR,$$
$$R = \begin{bmatrix} r \\ s \end{bmatrix}, \quad U = \begin{bmatrix} il & i\psi^* \\ i\psi & -il \end{bmatrix}, \tag{A1}$$
$$V = \begin{bmatrix} il^2 - \frac{i}{2}|\psi|^2 & il\psi^* + \frac{1}{2}\frac{\partial \psi^*}{\partial t} \\ il\psi - \frac{1}{2}\frac{\partial \psi}{\partial t} & -il^2 + \frac{i}{2}|\psi|^2 \end{bmatrix},$$

where l is a complex eigenvalue. The linear system reduces to the original equation under the equality $R_{tx} = R_{xt}$.

We define the "first-order component functions" as follows:

$$r_{1j} = 2ie^{-ix/2}\sin(A_{jr} + iA_{ji}),$$
$$s_{1j} = 2e^{ix/2}\cos(B_{jr} + iB_{ji}), \tag{A2}$$

where functions A and B are in turn defined as

$$A_{jr} = \frac{1}{2}\left[\arccos\left(\frac{\kappa_j}{2}\right) + (t - t_j)\kappa_j - \frac{\pi}{2}\right],$$
$$B_{jr} = \frac{1}{2}\left[-\arccos\left(\frac{\kappa_j}{2}\right) + (t - t_j)\kappa_j - \frac{\pi}{2}\right], \tag{A3}$$
$$A_{ji} = B_{ji} = \frac{1}{2}\left[(x - x_j)\kappa_j\sqrt{1 - \frac{\kappa_j^2}{4}}\right],$$

with $\kappa_j = 2\sqrt{1 + l_j^2}$. The subscripts r and i refer to real and imaginary parts, respectively.

These component functions in Eq. (A2) are the solutions of Eq. (A1) when the eigenvalue is purely imaginary and ψ is equal to the plane-wave seeding solution $\psi_0 = e^{ix}$. They also serve as basic building blocks for the construction of higher-order solutions, where the number j uniquely identifies each component. In particular, each component denoted by j is described by a set of free parameters, the corresponding eigenvalue l_j, and coordinate shifts (x_j, t_j).

A first-order solution to the system in Eq. (A1) incorporates only one chosen set of free parameters and its corresponding r and s equations from Eq. (A2), denoted by $j = 1$. The first-order wave function thus is expressed as

$$\psi_1 = \psi_0 + \frac{2(l_1^* - l_1)s_{11}r_{11}^*}{|r_{11}|^2 + |s_{11}|^2}. \tag{A4}$$

An order $n > 1$ solution requires higher-order versions of the expressions for r and s. These are recursively generated [26,29] by

$$r_{np} = [(l_{n-1}^* - l_{n-1})s_{n-1,1}^* r_{n-1,1}s_{n-1,p+1}$$
$$+ (l_{p+n-1} - l_{n-1})|r_{n-1,1}|^2 r_{n-1,p+1}$$
$$+ (l_{p+n-1} - l_{n-1}^*)|s_{n-1,1}|^2 r_{n-1,p+1}]/$$
$$(|r_{n-1,1}|^2 + |s_{n-1,1}|^2),$$

$$s_{np} = [(l^*_{n-1} - l_{n-1})s_{n-1,1}r^*_{n-1,1}r_{n-1,p+1} + (l_{p+n-1} - l_{n-1})|s_{n-1,1}|^2 s_{n-1,p+1} + (l_{p+n-1} - l^*_{n-1})|r_{n-1,1}|^2 s_{n-1,p+1}]/(|r_{n-1,1}|^2 + |s_{n-1,1}|^2). \quad \text{(A5)}$$

The p subscript in Eq. (A5) is used purely for enumeration and does not necessarily refer to a particular set of parameters. For example, the second-order function r_{21} is built from first-order component functions r_{11}, s_{11}, r_{12}, and s_{12}, thus incorporating parameters from both the components denoted by $j = 1,2$. Similarly, the third-order function r_{31} involves the second-order functions r_{21}, s_{21}, r_{22}, and s_{22}, which, in turn, are based on r_{11}, s_{11}, r_{12}, s_{12}, r_{13}, and s_{13} at the lowest order of recursion. Therefore, r_{31} constitutes parameters from all three components denoted by $j = 1,2,3$. In this way, Eq. (A5) allows n sets of free parameters to be incorporated into an order n solution. The diagram in Fig. 2.2 of Ref. [29] can be of use in representing this sequence of calculations. Subsequently, the order n NLSE solution is generated through recursion by

$$\psi_n = \psi_{n-1} + \frac{2(l^*_n - l_n)s_{n1}r^*_{n1}}{|r_{n1}|^2 + |s_{n1}|^2}. \quad \text{(A6)}$$

From a numerical perspective, the appearance of rogue-wave solutions can be determined by using values of κ_j that are as close to zero as computationally feasible. In this work, it is vital that individual κ_j values are still in a predetermined ratio, no matter how small they are. Shifts x_j and t_j are also dependent on powers of κ_j, via Eq. (2), and will likewise be close to zero.

[1] J. Cartwright and H. Nakamura, Notes Rec. Roy. Soc. **63**, 119 (2009).
[2] C. Kharif, E. Pelinovsky, and A. Slunyaev, *Rogue Waves in the Ocean* (Springer, Berlin, 2009).
[3] D. Peregrine, J. Austral. Math. Soc. Ser. B **25**, 16 (1983).
[4] N. Akhmediev, V. M. Eleonskii, and N. E. Kulagin, Zh. Eksp. Teor. Fiz. **89**, 1542 (1985) [Sov. Phys. JETP **62**, 894 (1985)].
[5] N. Akhmediev, A. Ankiewicz, and M. Taki, Phys. Lett. A **373**, 675 (2009).
[6] P. Dubard, P. Gaillard, C. Klein, and V. Matveev, Eur. Phys. J. Spec. Top. **185**, 247 (2010).
[7] P. Dubard and V. B. Matveev, Nat. Hazard Earth Syst. Sci. **11**, 667 (2011).
[8] P. Gaillard, J. Phys. A Math. Gen. **44**, 435204 (2011).
[9] Y. Ohta and J. Yang, Roy. Soc. Lond. Proc. Ser. A **468**, 1716 (2012).
[10] J. S. He, H. R. Zhang, L. H. Wang, K. Porsezian, and A. S. Fokas, Phys. Rev. E **87**, 052914 (2013).
[11] A. Chabchoub, N. P. Hoffmann, and N. Akhmediev, Phys. Rev. Lett. **106**, 204502 (2011).
[12] A. Chabchoub, N. P. Hoffmann, M. Onorato, and N. Akhmediev, Phys. Rev. X **2**, 011015 (2012).
[13] A. Chabchoub, N. Hoffmann, M. Onorato, A. Slunyaev, A. Sergeeva, E. Pelinovsky, and N. Akhmediev, Phys. Rev. E **86**, 056601 (2012).
[14] B. Kibler, J. Fatome, C. Finot, G. Millot, F. Dias, G. Genty, N. Akhmediev, and J. M. Dudley, Nat. Phys. **6**, 790 (2010).
[15] M. Erkintalo, K. Hammani, B. Kibler, C. Finot, N. Akhmediev, J. M. Dudley, and G. Genty, Phys. Rev. Lett. **107**, 253901 (2011).
[16] P. Shukla and W. Moslem, Phys. Lett. A **376**, 1125 (2012).
[17] R. Sabry, W. M. Moslem, and P. K. Shukla, Phys. Rev. E **86**, 036408 (2012).
[18] A. Ankiewicz, D. J. Kedziora, and N. Akhmediev, Phys. Lett. A **375**, 2782 (2011).
[19] D. J. Kedziora, A. Ankiewicz, and N. Akhmediev, Phys. Rev. E **84**, 056611 (2011).
[20] D. J. Kedziora, A. Ankiewicz, and N. Akhmediev, Phys. Rev. E **86**, 056602 (2012).
[21] D. J. Kedziora, A. Ankiewicz, and N. Akhmediev, Phys. Rev. E **85**, 066601 (2012).
[22] V. B. Matveev and M. Salle, *Darboux Transformations and Solitons* (Springer-Verlag, Berlin/Heidelberg, 1991).
[23] A. Ankiewicz, J. M. Soto-Crespo, and N. Akhmediev, Phys. Rev. E **81**, 046602 (2010).
[24] U. Bandelow and N. Akhmediev, Phys. Lett. A **376**, 1558 (2012).
[25] N. Akhmediev and N. V. Mitskevich, IEEE J. Quantum Electron. **27**, 849 (1991).
[26] N. Akhmediev, J. M. Soto-Crespo, and A. Ankiewicz, Phys. Lett. A **373**, 2137 (2009).
[27] N. Akhmediev, A. Ankiewicz, and J. M. Soto-Crespo, Phys. Rev. E **80**, 026601 (2009).
[28] A. Calini and C. Schober, Phys. Lett. A **298**, 335 (2002).
[29] N. Akhmediev and A. Ankiewicz, *Solitons: Nonlinear Pulses and Beams*, Vol. 5 of Optical and Quantum Electronics (Chapman & Hall, London, 1997), Chaps. 3–4.